Letter

Rhombic skyrmion lattice coupled with orthorhombic structural distortion in $EuAl_4$

Masaki Gen,[1,2,*] Rina Takagi,[2,3,4,5] Yoshito Watanabe,[1] Shunsuke Kitou,[2] Hajime Sagayama,[6] Naofumi Matsuyama,[7] Yoshimitsu Kohama,[7] Akihiko Ikeda,[8] Yoshichika Ōnuki,[2] Takashi Kurumaji,[1] Taka-hisa Arima,[1,2] and Shinichiro Seki[2,3,4]

[1]*Department of Advanced Materials Science, University of Tokyo, Kashiwa 277-8561, Japan*
[2]*RIKEN Center for Emergent Matter Science (CEMS), Wako 351-0198, Japan*
[3]*Institute of Engineering Innovation, University of Tokyo, Tokyo 113-0032, Japan*
[4]*Department of Applied Physics, University of Tokyo, Tokyo 113-8656, Japan*
[5]*PRESTO, Japan Science and Technology Agency (JST), Kawaguchi 332-0012, Japan*
[6]*Institute of Materials Structure Science, High Energy Accelerator Research Organization, Tsukuba 305-0801, Japan*
[7]*Institute for Solid State Physics, University of Tokyo, Kashiwa 277-8581, Japan*
[8]*Department of Engineering Science, University of Electro-Communications, Chofu, Tokyo 182-8585, Japan*

(Received 28 September 2022; revised 3 January 2023; accepted 10 January 2023; published 25 January 2023)

The centrosymmetric tetragonal itinerant magnet $EuAl_4$ exhibits an intricate magnetic phase diagram including rhombic and square skyrmion-lattice (SkL) phases in the external magnetic field. Here, we report a multi-axis dilatometric investigation of $EuAl_4$ by means of a newly designed fiber-Bragg-grating technique complemented by a resonant x-ray scattering experiment, revealing anisotropic magnetostriction and magnetovolume effect associated with successive phase transitions. The rhombic and square SkL phases are found to possess ∼0.10% and ∼0.03% orthorhombic structural distortion within the *ab* plane, respectively. We propose that the coupling between the spin system and the lattice deformation should be essential for the structural instability in $EuAl_4$, yielding a rich variety of topological spin textures with spontaneous rotational-symmetry breaking as well as a potential controllability of the SkL phases by uniaxial stress or pressure.

DOI: 10.1103/PhysRevB.107.L020410

Introduction. Spontaneous rotational-symmetry breaking (SRSB) has long been a central issue in condensed-matter physics. A prominent recent topic is the electronic nematicity observed in heavy-fermion compounds [1], topological kagome metals [2], and copper/iron-based high-T_c superconductors [3,4], where the contribution of electron-phonon coupling has often been controversial. The SRSB is more widely seen with the onset of a magnetic long-range order. In the presence of magnetic frustration, the mutual coupling of spin and lattice degrees of freedom can induce a magnetostructural transition with crystal symmetry lowering [5], as observed in solid oxygen [6,7] and pyrochlore-based antiferromagnets [8,9].

A magnetic skyrmion, a particlelike swirling spin texture, offers a fertile playground to explore emergent electromagnetic responses and transport properties [10–15]. In bulk crystals, skyrmions are usually arranged periodically, forming a skyrmion lattice (SkL) with high rotational symmetry. In the framework of the Ginzburg-Landau theory, a triangular SkL, characterized by a triple-**Q** modulation with hexagonal symmetry, can be stabilized by the external magnetic field and entropy effect [16–18]. This was observed in a number of chiral [18–23] and polar [24,25] magnets with the Dzyaloshinskii-Moriya (DM) interaction. Subsequently, the SkL was also discovered in rare-earth-based centrosymmetric itinerant magnets [26–30], whose magnetism is governed by the Ruderman-Kittel-Kasuya-Yosida (RKKY) interaction. Several mechanisms such as thermal fluctuations [31], higher-order multiple-spin interaction [32,33], single-ion anisotropy [34–36], dipole-dipole interaction [37,38], double-exchange mechanism [39], and interorbital frustration [40] are proposed as key ingredients for stabilizing the SkL in these compounds. It should be noted that the RKKY interaction is highly dependent on the shape of the Fermi surface. In fact, skyrmions in a tetragonal magnet $GdRu_2Si_2$ are arranged not in a triangular, but a square lattice [28,29].

Recently, the SRSB of SkL was discovered in a binary intermetallic $EuAl_4$ [30], which crystallizes in a centrosymmetric tetragonal structure (space group $I4/mmm$) with a square lattice of localized spin-7/2 Eu^{2+} ions. Figure 1(a) shows the magnetic-field-versus-temperature (H-T) phase diagram for $H \parallel [001]$, where seven magnetic phases (I–VII) appear, as well as the paramagnetic (PM) and the forced ferromagnetic (FM) phases [30,41]. In zero magnetic field, four magnetic transitions from the PM phase to phases VII, VI, V, and I take place at $T_{N1} = 15.4$ K, $T_{N2} = 13.2$ K, $T_{N3} = 12.2$ K, and $T_{N4} = 10.0$ K, respectively [30,41–46]. The former two are of the second order, whereas the latter two are of the first order. A single-crystal x-ray diffraction (XRD) study revealed a tetragonal-to-orthorhombic structural transition with the B_{1g}-type distortion at T_{N3} [43]. When applying a magnetic field along [001], successive metamagnetic

*masaki.gen@riken.jp

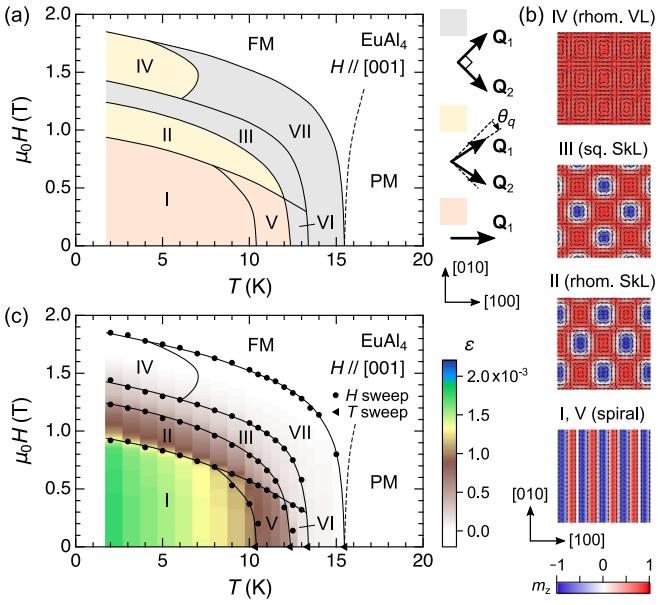

FIG. 1. (a) H-T phase diagram of $EuAl_4$ for $H \parallel [001]$, which is an excerpt from Refs. [30,41] and reproduced in the present work. PM and FM represent paramagnetic and ferromagnetic phases, respectively. The fundamental modulation vectors in each phase are depicted on the right side. (b) Schematics of the real-space spin configurations in phases I–V. (c) Contour plots of the orthorhombic structural distortion $\varepsilon = (b-a)/a_0$ mapped on the H-T phase diagram revealed in this study. ε is set to zero at 0 T and 18 K. Closed circles (triangles) indicate transition fields (temperatures at 0 T) determined from peaks in $\partial\varepsilon/\partial H$ ($\partial\varepsilon/\partial T$). The phase boundary between phases IV and VII was not resolved in our magnetostriction measurements.

transitions from phase I to II, III, and IV take place below 5 K. A small-angle neutron scattering experiment [30] unveiled the magnetic structures of all these phases: phases I and V are single-**Q** screw spiral with $\mathbf{Q}_1 = (0.19, 0, 0)$ and $(0.17, 0, 0)$, respectively; phases II and III are double-**Q** SkL; phases IV and VII are double-**Q** vortex-antivortex lattice (VL); and phase VI is double-**Q** meron-antimeron lattice (ML). Two fundamental modulation vectors in phases III, VI, and VII are $\mathbf{Q}_1 = (q, q, 0)$ and $\mathbf{Q}_2 = (q, -q, 0)$, where $q \sim 0.085$, so that the spin textures possess fourfold symmetry. In phases II and IV, on the other hand, $\mathbf{Q}_1$ and $\mathbf{Q}_2$ are tilted by $\theta_q \sim 5^\circ$ toward the [100] direction, resulting in the rhombic SkL and VL, respectively [Fig. 1(b)]. In short, the SRSB is observed even in the double-**Q** states (II and IV) as well as in the single-**Q** states (I and V).

Theoretically, a *rectangular* SkL with fourfold symmetry breaking can appear on a square-lattice spin model by incorporating the competition among exchange interactions in momentum space $J_{\mathbf{Q}}$ with $\mathbf{Q}_1 = (q, q, 0)$, $\mathbf{Q}_2 = (q, -q, 0)$, and their higher harmonics, $\mathbf{Q}_1 + \mathbf{Q}_2$ and $\mathbf{Q}_1 - \mathbf{Q}_2$ [47,48], though this picture is incompatible with the *rhombic* SkL with tilted two-**Q** vectors in $EuAl_4$. Recalling the structural transition at T_{N3}, it is natural to anticipate that the spin-lattice coupling is responsible for stabilizing the rhombic double-**Q** modulation in phases II and IV. To shed light on this, it is important to clarify the in-field crystal-structure changes. Dilatometry using the capacitance method has sufficient sensitivity, and a previous study [41] succeeded in observing the relative change in the lattice constant a on a detwinned crystal of $EuAl_4$ while the information on the lattice constants b and c was lacking (we define $a < b$ below T_{N3}). Besides, the correspondence between the orthorhombic distortion and **Q** vectors has yet been revealed.

In this Letter, we investigate the lattice constant changes for three principal axes associated with the field-induced phase transitions in $EuAl_4$, unveiling anisotropic magnetostriction and magnetovolume effect. Figure 1(c) shows a contour plot of the orthorhombic structural distortion ε mapped on the H-T phase diagram: e.g., $\sim$0.10% and $\sim$0.03% structural distortion is found at 2 K in the rhombic and square SkL phases, respectively. We also performed a resonant x-ray scattering (RXS) experiment, revealing that the **Q** vector is oriented along the elongated b axis in the single-**Q** spiral phase (phase I). Based on the microscopic consideration of a spin model, we propose that the spin-lattice coupling should act as the principal driving force for the multiple magnetostructural transitions and the SRSB of SkL in $EuAl_4$.

Methods. Single crystals of $EuAl_4$ were synthesized by the Al self-flux method as in Ref. [30]. The as-grown crystals were cut into the rectangular parallelepiped shape. The magnetization was measured using a commercial magnetometer (Magnetic Property Measurement System, Quantum Design). The dilatometry measurements were performed by the fiber-Bragg-grating (FBG) method using an optical sensing instrument (Hyperion si155, LUNA). The relative sample-length changes $\Delta L/L_0$ along [100] and [001] were simultaneously measured, as illustrated in Fig. 2(a). A sample with two FBGs was loaded in a cryostat equipped with a superconducting magnet (Spectromag, Oxford Instruments). For experimental details, see the Supplemental Material [49]. Throughout this Letter, we define Δk ($k = L, a, b, c$) as $\Delta k \equiv k - k_0$, with the baseline value k_0 at 0 T and 18 K, and assume $a_0 = b_0$. The RXS measurement was performed at BL-3A, Photon Factory, KEK, Japan, by using incident x rays in resonance with an Eu L_2 absorption edge (7.615 keV). A crystal with a flat (100) plane was attached on an Al plate using GE varnish and loaded into a cryostat equipped with a vertical-field superconducting magnet, where the scattering plane was set to be $(H, K, 0)$. In all the experiments, a magnetic field was applied along [001].

Results. The zero-field thermal expansion profiles measured along [100], $(\Delta L/L_0)_1$ and $(\Delta L/L_0)_2$, which were taken in independent sample settings, are shown by cyan lines in Fig. 2(b), along with the temperature evolution of $\Delta a/a_0$ and $\Delta b/b_0$ revealed by the previous XRD study [43] (open circles). Opposite behaviors are observed between $(\Delta L/L_0)_1$ and $(\Delta L/L_0)_2$ below T_{N3}: a positive thermal expansion for $(\Delta L/L_0)_1$, while negative for $(\Delta L/L_0)_2$. This discrepancy should be attributed to the difference in the crystallographic-domain patterns around the local area where the FBG was glued in each setting [Fig. 2(c)]. Assuming $(\Delta L/L_0)_i = (1 - p_i)(\Delta a/a_0) + p_i(\Delta b/b_0)$, we determine $p_1 = 0.49$ for $(\Delta L/L_0)_1$ and $p_2 = 0.74$ for $(\Delta L/L_0)_2$ so that they match the XRD data at 6.3 K. Importantly, p_i is reproduced no matter how many times the temperature or magnetic field is repeatedly scanned in our experiments

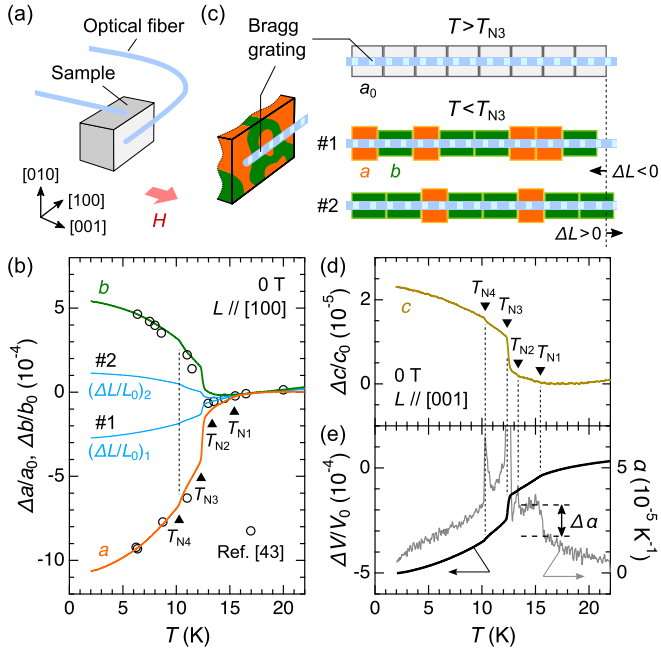

FIG. 2. (a) Schematic of the sample setting of FBG experiments, where $\Delta L/L_0$ along [100] and [001] are simultaneously measured by adhering two optical fibers to one crystal orthogonally. (b) Thermal expansion measured along [100] in zero field (cyan lines): $(\Delta L/L_0)_1$ [$(\Delta L/L_0)_2$] for setting 1 [setting 2]. Open circles are extracted from the lattice constants a and b reported in Ref. [43]. $\Delta a/a_0$ and $\Delta b/b_0$ are calculated by $(\Delta L/L_0)_1$, $(\Delta L/L_0)_2$, and the volume ratio of the crystallographic domains $(1-p_i):p_i$ with $p_1 = 0.49$ ($p_2 = 0.74$) for setting 1 (setting 2). (c) Schematic of the crystallographic domains distribution in the (001) plane below T_{N3}. (d) Thermal expansion measured along [001] in zero field ($\Delta c/c_0$). (e) Volume thermal expansion (left axis) and its temperature derivative (right axis) in zero field. All the thermal expansion data were obtained in the warming process.

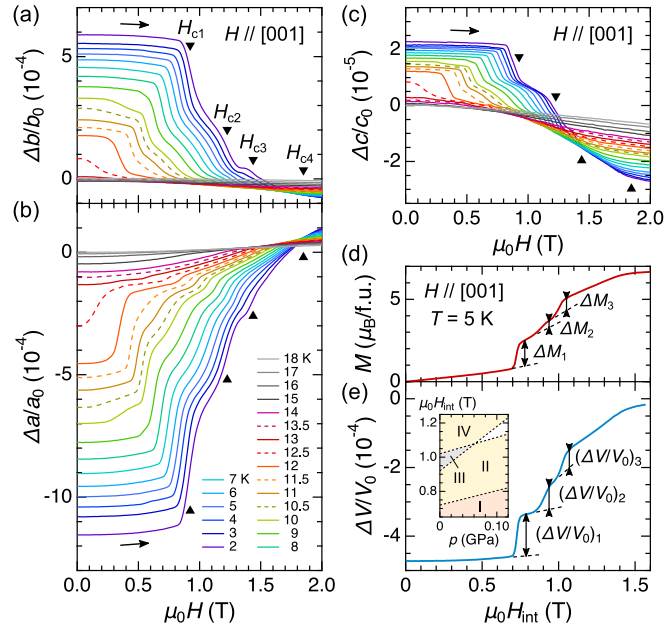

FIG. 3. (a)–(c) Magnetic-field evolution of the lattice constant changes (a) $\Delta b/b_0$, (b) $\Delta a/a_0$, and (c) $\Delta c/c_0$ for $H \parallel [001]$. The color scale of temperature is shown in the inset of (b). Triangles denote magnetic transitions at 2 K. (d) Magnetization and (e) volume magnetostriction curves for $H \parallel [001]$ at 5 K. The horizontal axis $H_{\rm int}$ represents the magnetic field after demagnetization correction. The inset in (e) shows the thermodynamically predicted H-p phase diagram. All the magnetostriction and magnetization data were obtained in the field-increasing process.

(Fig. S2 in the Supplemental Material [49]). Thanks to this feature, we can decompose $\Delta a/a_0$ and $\Delta b/b_0$ from the two experimental data sets $(\Delta L/L_0)_1$ and $(\Delta L/L_0)_2$ in the whole measured H-T region using the following relations: $\Delta a/a_0 = [p_2(\Delta L/L_0)_1 - p_1(\Delta L/L_0)_2]/(p_2 - p_1)$ and $\Delta b/b_0 = [-(1-p_2)(\Delta L/L_0)_1 + (1-p_1)(\Delta L/L_0)_2]/(p_2 - p_1)$. The calculated $\Delta a/a_0$ and $\Delta b/b_0$ as a function of temperature are shown by orange and green lines in Fig. 2(b), respectively, which agree well with the XRD data.

As shown in Fig. 2(d), the observed $\Delta L/L_0$ along [001], which corresponds to $\Delta c/c_0$, exhibits negative thermal expansion below T_{N1}. The entire change in $\Delta c/c_0$ across the phase transitions is much smaller than those in $\Delta a/a_0$ and $\Delta b/b_0$. This trend is in contrast to $GdRu_2Si_2$ [53] and suggests the weak out-of-plane spin-lattice coupling in $EuAl_4$. We double check the reliability of our measurements by estimating thermodynamic quantities. Figure 2(e) shows the volume thermal expansion calculated as $\Delta V/V_0 = \Delta a/a_0 + \Delta b/b_0 + \Delta c/c_0$ and its temperature derivative $\alpha \equiv \partial(\Delta V/V_0)/\partial T$. α jumps by $\Delta\alpha \approx -1.5 \times 10^{-4}$ K^{-1} at T_{N1}. By adopting this value in combination with the reported specific-heat change $\Delta C_p \approx -6$ J/(K mol) at T_{N1} [41,42] and the volume $V \approx 107.1$ Å^3/f.u. at 20 K [54] to the Ehrenfest relation $\partial T_N/\partial p = T_N V(\Delta\alpha/\Delta C_p)$, the pressure p dependence of T_{N1} is estimated to 2.5 K/GPa. This estimation agrees well with the previously obtained value $\partial T_{N1}/\partial p = 2.24$ K/GPa [42].

Having confirmed the validity of our experimental and analytical methods from the thermal expansion data, we investigate the field-induced crystal-structure changes of $EuAl_4$. Figures 3(a)–3(c) show magnetostriction curves for $H \parallel [001]$ measured at various temperatures. We obtain the field evolution of $\Delta a/a_0$ and $\Delta b/b_0$ by the same procedure described above (Fig. S1 in the Supplemental Material [49]). As the magnetic field increases at 2 K, $\Delta a/a_0$ monotonically increases, accompanied by jumps at first-order transitions at H_{c1}, H_{c2}, and H_{c3} in accord with Ref. [41]. In contrast, $\Delta b/b_0$ and $\Delta c/c_0$ monotonically decrease, indicating that the structural distortion associated with the magnetic ordering is gradually suppressed toward higher fields. Furthermore, we performed similar sets of thermal expansion and magnetostriction measurements for $\Delta L/L_0 \parallel [100]$ on a crystal nearly detwinned by applying the thermal stress (Fig. S3 in the Supplemental Material [49]); the observed $\Delta L/L_0$ is close to $\Delta b/b_0$ and reasonably consistent with Figs. 2(b) and 3(a), while a uniaxial stress effect is seen in a shift of structural transition temperatures T_{N3} and T_{N4} by more than 1 K. ε calculated by $\Delta b/b_0 - \Delta a/a_0$ is visualized on the H-T phase diagram in Fig. 1(c). Note that ε may be slightly underestimated in high-field and high-temperature sides due to the missing incorporation of possible slight orthorhombic

distortion at 0 T and 18 K [54] in our analysis (for details, see the Supplemental Material [49]).

Our magnetostriction data provide insights on the pressure effect on the stability of the rhombic and square SkL phases. Figures 3(d) and 3(e) show magnetization and volume magnetostriction curves, respectively, for $H \parallel [001]$ at 5 K. Here, the demagnetization is corrected so as to accurately estimate the magnitudes of the magnetization jumps at H_{c1}, H_{c2}, and H_{c3}: $\Delta M_1 \approx 1.6\ \mu_B$/f.u., $\Delta M_2 \approx 0.3\ \mu_B$/f.u., and $\Delta M_3 \approx 0.6\ \mu_B$/f.u., respectively. The corresponding volume jumps are $(\Delta V/V_0)_1 \approx 1.2 \times 10^{-4}$, $(\Delta V/V_0)_2 \approx 0.7 \times 10^{-4}$, and $(\Delta V/V_0)_3 \approx 0.5 \times 10^{-4}$, respectively. According to Clausius-Clapeyron's equation $\partial(\mu_0 H_c)/\partial p = \Delta V/\Delta M$, the pressure dependence of each critical field is estimated to $\partial(\mu_0 H_{c1})/\partial p \approx 0.8$, $\partial(\mu_0 H_{c2})/\partial p \approx 2.6$, and $\partial(\mu_0 H_{c3})/\partial p \approx 1.0$ T/GPa. A relatively large value of $\partial(\mu_0 H_{c2})/\partial p$ is attributed to the substantial volume expansion at the transition to phase III in spite of the small magnetization jump. The predicted H-p phase diagram is shown in the inset of Fig. 3(e), suggesting that the square SkL can be annihilated by applying hydrostatic pressure lower than 0.1 GPa. The stability of each SkL phase may also be controllable by tuning the chemical pressure such as the isovalent Ga substitution for Al [55], which should act as the negative pressure. Indeed, the H-T phase diagrams of $EuGa_4$ and $EuGa_2Al_2$ are simpler than that of $EuAl_4$ [56,57], presumably suggesting the absence of orthorhombic structural distortion and the rhombic SkL phase in these compounds. A systematic investigation of the phase diagram of the $Eu(Ga_{1-x}Al_x)_4$ system would be intriguing.

To reveal the one-to-one correspondence between the orthorhombic structural distortion and magnetic modulation, we performed the RXS experiment to observe both the fundamental 400 and magnetic Bragg reflections. Figure 4(a) shows the schematic of the observed reflections around (4, 0, 0) on the $(H, K, 0)$ scattering plane at 5 K in zero field. The corresponding intensity profiles in the $(H, 0, 0)$ and $(4, K, 0)$ scans are shown in the upper and lower panels, respectively, in Fig. 4(b). As shown in the inset of Fig. 4(b), we observe a peak splitting for the 400 reflection. The estimated lattice constants are $a = 4.3748$ Å and $b = 4.3836$ Å, yielding $\varepsilon = 2.0 \times 10^{-3}$. This value is a bit larger than that obtained in the previous XRD, $\varepsilon = 1.6 \times 10^{-3}$ [43], presumably owing to the extrinsic strain caused by the thermal expansion mismatch between the $EuAl_4$ crystal and the Al substrate in our RXS experiment. Importantly, the magnetic peaks are observed at $(4 - \delta - q, 0, 0)$, $(4 - \delta + q, 0, 0)$, $(4, -q, 0)$, and $(4, q, 0)$ with $\delta = 0.002$ and $q = 0.194$. This indicates that the magnetic peaks at the former (latter) two originate from the fundamental peak observed at $(4 - \delta, 0, 0)$ [$(4, 0, 0)$]. Accordingly, we conclude that the **Q** vector in phase I is oriented along the elongated b axis.

Figures 4(c)–4(e) summarize the field evolutions of the crystal structure in the ab plane and the corresponding magnetic modulations, both of which are obtained during the same field-increasing process in the RXS experiment. In Fig. 4(e), q_a (q_b) represent the a (b) component of $\mathbf{Q}_1$, as shown in Fig. 4(f) ($q_a = 0$ in phase I). The observed q_a and q_b well reproduce the previous neutron study [30]. Below $\mu_0 H_{c2} \approx 1.05$ T, the magnitude of the 400 peak splitting is larger than each peak width so that we can derive ε as well as the lattice constants a and b by the double-Lorentzian fit on the intensity

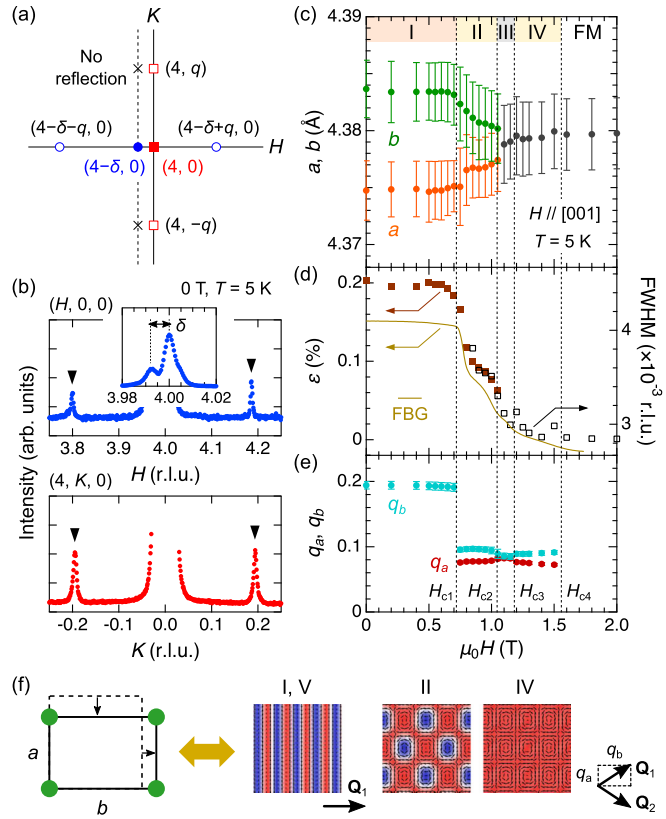

FIG. 4. Results of the RXS experiment performed at 5 K. (a) Schematic of the observed fundamental and magnetic Bragg reflections in zero field drawn on the scattering plane. (b) Intensity profiles in the $(H, 0, 0)$ and $(4, K, 0)$ scans in zero field. The inset shows the splitting pattern of the fundamental 400 reflection. (c)–(e) Magnetic-field evolutions of (c) the lattice constants a and b, (d) the orthorhombic structural distortion ε obtained from the RXS (symbols) and FBG experiments (solid line) [58], and (e) the a and b components of the **Q** vector. In (c) and (e), vertical bars represent ranges on real space corresponding to FWHMs of the fitting functions for the RXS intensity profiles [59]. In (d), filled squares indicate ε derived from a and b shown in (c) (left axis), and open squares indicate the FWHM of a single Lorentzian function fitted on the 400 peak (right axis). (f) Correspondence between the orthorhombic distortion and magnetic structure in phases I, II, IV, and V.

profile [Figs. 4(c) and 4(d)]. a and b remains almost constant up to $\mu_0 H_{c1} \approx 0.75$ T, followed by an abrupt increase in a and decrease in b. On entering phase II, ε decreases to 1.0×10^{-3} and gets even smaller with increasing the magnetic field. Above H_{c2}, the 400 peak splitting is invisible within instrument resolution, so that we plot the averaged lattice constant obtained from the single-Lorentzian fit on the intensity profile in Fig. 4(c). The FWHM of the fitting function above H_{c2} represents a gradual decrease from phase III to the FM phase [Fig. 4(d)], suggesting that slight orthorhombic distortion remains in phases III and IV. The correspondence between the crystal structure and spin textures with fourfold symmetry breaking is depicted in Fig. 4(f).

Discussions. To understand the magnetic instability in $EuAl_4$, we start from a classical Heisenberg model on a simple square lattice: $\mathcal{H} = \sum_{\langle i,j \rangle_k} J_k \mathbf{S}_i \cdot \mathbf{S}_j + \mathcal{H}_{ex}$. Here, $J_1 <$

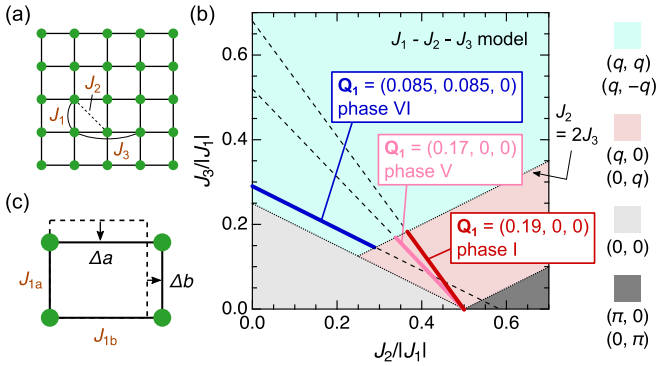

FIG. 5. (a) Exchange interactions up to the third NN on a square lattice. (b) Exchange parameter sets of J_2 and J_3 consistent with the fundamental $\mathbf{Q}$ vectors for phases VI, V, and I in zero field. The phase diagram is an excerpt from Ref. [60] (see text for details). (c) Tetragonal-to-orthorhombic distortion on a square lattice, resulting in inequivalent NN exchanges $J_{1a} \approx J_1 + (dJ_1/dr)\Delta a$ and $J_{1b} \approx J_1 + (dJ_1/dr)\Delta b$, where $dJ_1/dr > 0$.

0, $J_2 > 0$, and $J_3 > 0$ are the exchange interactions up to the third-nearest neighbor (NN) [Fig. 5(a)], which originates from the RKKY interaction in $EuAl_4$. This model can host various kinds of single-$\mathbf{Q}$ and multiple-$\mathbf{Q}$ spin textures depending on the extra terms $\mathcal{H}_{ex}$; e.g., the double-$\mathbf{Q}$ ML is stabilized in the presence of the single-ion anisotropy and compass anisotropy [60], which would be relevant to phase VI in $EuAl_4$ [30]. If we neglect $\mathcal{H}_{ex}$, incommensurate ordering vectors $\mathbf{Q} = (\pm q, \pm q, 0)$ with $q = \arccos(-\frac{J_1}{2J_2+4J_3})$ are selected for $2J_3 > J_2$ whereas $\mathbf{Q} = (\pm q, 0, 0)$ or $(0, \pm q, 0)$ with $q = \arccos(-\frac{J_1+2J_2}{4J_3})$ for $J_2 > 2J_3$ [60]. The exchange parameter sets that agree with the $\mathbf{Q}$ vectors for the zero-field phases VI, V, and I [30,45] are plotted in a parameter space of $J_2/|J_1|$ and $J_3/|J_1|$ in Fig. 5(b). As phases VI, V, and I should compete with each other within a small energy scale, $(J_2/|J_1|, J_3/|J_1|) \approx (0.3, 0.15)$ is a reasonable parameter position for $EuAl_4$. We note that the $\mathbf{Q}$ switching at T_{N3} and T_{N4} cannot occur within the frozen J_1–J_2–J_3 model.

Here we propose the spin-lattice coupling as a driving force to modify J_1 through a magnetostructural transition. This mechanism is reasonable to consider in $EuAl_4$ on the basis of the observed exceptionally large thermal expansion and magnetostriction associated with the magnetic transitions ($\sim 10^{-3}$) compared to those in other SkL-hosting chiral magnets [61] and Eu/Gd-based itinerant magnets ($\sim 10^{-5}$–10^{-4}) [53,62,63]. This collective phenomenon is known as the spin Jahn-Teller effect, where the magnetic frustration is relieved by favoring one of the competing exchange interactions through the lattice distortion [5]. The B_{1g}-type distortion is selected below T_{N3} [43], indicating that the FM J_1 along the a and b axes become inequivalent: $J_{1a} \approx J_1 + (dJ_1/dr)\Delta a$ and $J_{1b} \approx J_1 + (dJ_1/dr)\Delta b$, respectively [Fig. 5(c)]. As the $\mathbf{Q}$ vector is oriented along the b axis at 5 K according to the RXS experiment, FM coupling is stronger for the shorter a axis, so that $dJ_1/dr > 0$. This picture is compatible with the $\mathbf{Q}$ switching from (0.085, 0.085, 0) to (0.17, 0, 0) at T_{N3} because the total exchange energy can be reduced for the latter after the modification of J_1. The additional first-order transition from phase V to I at T_{N4}, where a modulation period changes from $q = 0.17$ to 0.19 while conserving its orientation, suggests the competition of these two spiral states in the presence of the spin-lattice coupling; phase I is eventually stabilized as a ground state by enhancing the orthorhombic structural distortion and consequently increasing $J_2/|J_{1b}|$. We note that a uniaxial stress should facilitate the magnetostructural transitions at T_{N3} and T_{N4} because the system can save the elastic energy, which is indeed observed as mentioned above (Fig. S3 in the Supplemental Material [49]).

The importance of the spin-lattice coupling is also corroborated from the strong correlation between the in-field spin textures and orthorhombic structural distortion. In the rhombic SkL phase (II), two fundamental $\mathbf{Q}$ vectors are tilted from $\mathbf{Q}_1 = (q, q, 0)$ and $\mathbf{Q}_2 = (q, -q, 0)$ ($q \sim 0.085$) by $\theta_q \sim 5^\circ$ [30]. As can be seen from Fig. 1(c), a large structural distortion $\varepsilon \sim 1.0 \times 10^{-3}$ exists in phase II like in phase V, suggesting the importance of the spin-lattice coupling on stabilizing the rhombic-$\mathbf{Q}$ modulation. It is worth referring that in a cubic chiral magnet FeGe 0.3% uniaxial strain deforms the triangular SkL by 20% owing to the anisotropic modulation of the DM interaction [64]. In the rhombic SkL in $EuAl_4$, comparable structural distortion and SkL deformation are spontaneously induced, i.e., without applying the mechanical force. Even in the square SkL phase (III), a moderate structural distortion $\varepsilon \sim 3 \times 10^{-4}$ is found [Fig. 1(c)], indicating that J_{1a} and J_{1b} remain inequivalent. Such a deviation from the tetragonal symmetry in phase III might be observed as a slight difference in q_a and q_b in our RXS data [Fig. 4(e)]. Interestingly, a reentrant symmetry breaking of the spin texture is seen in the high-field rhombic VL phase (IV), though the orthorhombic structural distortion seems monotonically suppressed toward higher fields [Figs. 4(d) and 4(e)]. The reason why the VL is more prone to deformation (in terms of spin textures) than the SkL is elusive at this stage. The investigation on the anisotropic elastic property by means of ultrasonic measurements [65,66] would deepen our understanding on the SRSB of the SkL and VL in $EuAl_4$. In addition, a theoretical framework incorporating local phonon modes or inequivalent J_{1a} and J_{1b} on the square lattice would be a promising approach to reproduce versatile magnetic phases in $EuAl_4$.

Conclusion. In summary, we have comprehensively revealed the crystal-structure changes of $EuAl_4$ associated with the field-induced phase transitions to address the microscopic origin of the SRSB of SkL. The amplitudes of the orthorhombic structural distortion are quantitatively estimated for each magnetic phase. We also unveil the correlation between magnetic modulation and the underlying crystal-structure distortion. The appearance of two types of SkL phases should originate from the magnetic frustration in momentum space coupled with the lattice degrees of freedom. Furthermore, the orthorhombic structural distortion accompanies a pronounced magnetovolume effect. $EuAl_4$ would be an ideal playground to explore the tunability of the SkL phases by pressure as well as uniaxial stress.

Acknowledgments. The authors appreciate S. Hayami and H. Yoshimochi for fruitful discussions. The authors appreciate S. Shimomura for providing the data of the lattice constants of $EuAl_4$ in Ref. [43]. This work was financially supported by the JSPS KAKENHI Grants-In-Aid for Scientific Research

(Grants No. 19H01835, No. JP19H05826, No. 20H00349, No. 20J10988, No. 21H04440, No. 21H04990, No. 21K13876, No. 21K18595, No. 22H04965, No. 22K14010), PRESTO (Grant No. JPMJPR20B4), and Asahi Glass Foundation. The resonant x-ray scattering experiment at PF was performed under the approval of the Photon Factory Program Advisory Committee (Proposal No. 2022G551). M.G. was a postdoctoral research fellow of the JSPS.

[1] R. Okazaki, T. Shibauchi, H. J. Shi, Y. Haga, T. D. Matsuda, E. Yamamoto, Y. Onuki, H. Ikeda, and Y. Matsuda, Rotational symmetry breaking in the hidden-order phase of URu_2Si_2, Science **331**, 439 (2011).

[2] L. Nie, K. Sun, W. Ma, D. Song, L. Zheng, Z. Liang, P. Wu, F. Yu, J. Li, M. Shan, D. Zhao, S. Li, B. Kang, Z. Wu, Y. Zhou, K. Liu, Z. Xiang, J. Ying, Z. Wang, T. Wu *et al.*, Charge-density-wave-driven electronic nematicity in a kagome superconductor, Nature (London) **604**, 59 (2022).

[3] M. J. Lawler, K. Fujita, J. Lee, A. R. Schmidt, Y. Kohsaka, C. K. Kim, H. Eisaki, S. Uchida, J. C. Davis, J. P. Sethna, and E.-A. Kim, Intra-unit-cell electronic nematicity of the high-T_c copper-oxide pseudogap states, Nature (London) **466**, 347 (2010).

[4] S. Kasahara, H. J. Shi, K. Hashimoto, S. Tonegawa, Y. Mizukami, T. Shibauchi, K. Sugimoto, T. Fukuda, T. Terashima, A. H. Nevidomskyy, and Y. Matsuda, Electronic nematicity above the structural and superconducting transition in $BaFe_2(As_{1-x}P_x)_2$, Nature (London) **486**, 382 (2012).

[5] C. Lacroix, P. Mendels, and F. Mila, *Introduction to Frustrated Magnetism* (Springer, Heidelberg, 2011).

[6] G. C. DeFotis, Magnetism of solid oxygen, Phys. Rev. B **23**, 4714 (1981).

[7] P. W. Stephens and C. F. Majkrzak, Magnetic structure and dynamics in the α and β phases of solid oxygen, Phys. Rev. B **33**, 1 (1986).

[8] S.-H. Lee, C. Broholm, T. H. Kim, W. Ratcliff II, and S.-W. Cheong, Local Spin Resonance and Spin-Peierls-like Phase Transition in a Geometrically Frustrated Antiferromagnet, Phys. Rev. Lett. **84**, 3718 (2000).

[9] M. Matsuda, H. Ueda, A. Kikkawa, Y. Tanaka, K. Katsumata, Y. Narumi, T. Inami, Y. Ueda, and S.-H. Lee, Spin-lattice instability to a fractional magnetization state in the spinel $HgCr_2O_4$, Nat. Phys. **3**, 397 (2007).

[10] A. Neubauer, C. Pfleiderer, B. Binz, A. Rosch, R. Ritz, P. G. Niklowitz, and P. Böni, Topological Hall Effect in the *A* Phase of MnSi, Phys. Rev. Lett. **102**, 186602 (2009).

[11] F. Jonietz, S. Mühlbauer, C. Pfleiderer, A. Neubauer, W. Münzer, A. Bauer, T. Adams, R. Georgii, P. Böni, R. A. Duine, K. Everschor, M. Garst, and A. Rosch, Spin transfer torques in MnSi at ultralow current densities, Science **330**, 1648 (2010).

[12] T. Schulz, R. Ritz, A. Bauer, M. Halder, M. Wagner, C. Franz, C. Pfleiderer, K. Everschor, M. Garst, and A. Rosch, Emergent electrodynamics of skyrmions in a chiral magnet, Nat. Phys. **8**, 301 (2012).

[13] P.-J. Hsu, A. Kubetzka, A. Finco, N. Romming, K. von Bergmann, and R. Wiesendanger, Electric-field-driven switching of individual magnetic skyrmions, Nat. Nanotechnol. **12**, 123 (2017).

[14] M. Hirschberger, L. Spitz, T. Nomoto, T. Kurumaji, S. Gao, J. Masell, T. Nakajima, A. Kikkawa, Y. Yamasaki, H. Sagayama, H. Nakao, Y. Taguchi, R. Arita, T. Arima, and Y. Tokura, Topological Nernst Effect of the Two-Dimensional Skyrmion Lattice, Phys. Rev. Lett. **125**, 076602 (2020).

[15] M. Akazawa, H.-Y. Lee, H. Takeda, Y. Fujima, Y. Tokunaga, T. Arima, J. H. Han, and M. Yamashita, Topological thermal hall effect induced by magnetic skyrmions, Phys. Rev. Research **4**, 043085 (2022).

[16] A. N. Bogdanov and D. A. Yablonskii, Thermodynamically stable "vortices" in magnetically ordered crystals. The mixed state of magnets, Sov. Phys. JETP **68**, 101 (1989).

[17] A. Bogdanov and A. Hubert, Thermodynamically stable magnetic vortex states in magnetic crystals, J. Magn. Magn. Mater. **138**, 255 (1994).

[18] S. Mühlbauer, B. Binz, F. Jonietz, C. Pfleiderer, A. Rosch, A. Neubauer, R. Georgii, and P. Böni, Skyrmion lattice in a chiral magnet, Science **323**, 915 (2009).

[19] X. Z. Yu, Y. Onose, N. Kanazawa, J. H. Park, J. H. Han, Y. Matsui, N. Nagaosa, and Y. Tokura, Real-space observation of a two-dimensional skyrmion crystal, Nature (London) **465**, 901 (2010).

[20] X. Z. Yu, N. Kanazawa, Y. Onose, K. Kimoto, W. Z. Zhang, S. Ishiwata, Y. Matsui, and Y. Tokura, Near room-temperature formation of a skyrmion crystal in thin-films of the helimagnet FeGe, Nat. Mater. **10**, 106 (2011).

[21] S. Seki, X. Z. Yu, S. Ishiwata, and Y. Tokura, Observation of skyrmions in a multiferroic material, Science **336**, 198 (2012).

[22] Y. Tokunaga, X. Z. Yu, J. S. White, H. M. Rønnow, D. Morikawa, Y. Taguchi, and Y. Tokura, A new class of chiral materials hosting magnetic skyrmions beyond room temperature, Nat. Commun. **6**, 7638 (2015).

[23] K. Kaneko, M. D. Frontzek, M. Matsuda, A. Nakao, K. Munakata, T. Ohhara, M. Kakihana, Y. Haga, M. Hedo, T. Nakama, and Y. Onuki, Unique helical magnetic order and field-induced phase in trillium lattice antiferromagnet EuPtSi, J. Phys. Soc. Jpn. **88**, 013702 (2019).

[24] I. Kézsmárki, S. Bordács, P. Milde, E. Neuber, L. M. Eng, J. S. White, H. M. Rønnow, C. D. Dewhurst, M. Mochizuki, K. Yanai, H. Nakamura, D. Ehlers, V. Tsurkan, and A. Loidl, Néel-type skyrmion lattice with confined orientation in the polar magnetic semiconductor GaV_4S_8, Nat. Mater. **14**, 1116 (2015).

[25] T. Kurumaji, T. Nakajima, V. Ukleev, A. Feoktystov, T. Arima, K. Kakurai, and Y. Tokura, Néel-Type Skyrmion Lattice in the Tetragonal Polar Magnet $VOSe_2O_5$, Phys. Rev. Lett. **119**, 237201 (2017).

[26] T. Kurumaji, T. Nakajima, M. Hirschberger, A. Kikkawa, Y. Yamasaki, H. Sagayama, H. Nakao, Y. Taguchi, T. Arima, and Y. Tokura, Skyrmion lattice with a giant topological Hall effect in a frustrated triangular-lattice magnet, Science **365**, 914 (2019).

[27] M. Hirschberger, T. Nakajima, S. Gao, L. Peng, A. Kikkawa, T. Kurumaji, M. Kriener, Y. Yamasaki, H. Sagayama, H.

Nakao, K. Ohishi, K. Kakurai, Y. Taguchi, X. Z. Yu, T. Arima, and Y. Tokura, Skyrmion phase and competing magnetic orders on a breathing kagomé lattice, Nat. Commun. **10**, 5831 (2019).

[28] N. D. Khanh, T. Nakajima, X. Z. Yu, S. Gao, K. Shibata, M. Hirschberger, Y. Yamasaki, H. Sagayama, H. Nakao, L. Peng, K. Nakajima, R. Takagi, T. Arima, Y. Tokura, and S. Seki, Nanometric square skyrmion lattice in a centrosymmetric tetragonal magnet, Nat. Nanotechnol. **15**, 444 (2020).

[29] N. D. Khanh, T. Nakajima, S. Hayami, S. Gao, Y. Yamasaki, H. Sagayama, H. Nakao, R. Takagi, Y. Motome, Y. Tokura, T. Arima, and S. Seki, Zoology of multiple-Q spin textures in a centrosymmetric tetragonal magnet with itinerant electrons, Adv. Sci. **9**, 2105452 (2022).

[30] R. Takagi, N. Matsuyama, V. Ukleev, L. Yu, J. S. White, S. Francoual, J. R. L. Mardegan, S. Hayami, H. Saito, K. Kaneko, K. Ohishi, Y. Ōnuki, T. Arima, Y. Tokura, T. Nakajima, and S. Seki, Square and rhombic lattices of magnetic skyrmions in a centrosymmetric binary compound, Nat. Commun. **13**, 1472 (2022).

[31] T. Okubo, S. Chung, and H. Kawamura, Multiple-q States and the Skyrmion Lattice of the Triangular-Lattice Heisenberg Antiferromagnet under Magnetic Fields, Phys. Rev. Lett. **108**, 017206 (2012).

[32] R. Ozawa, S. Hayami, and Y. Motome, Zero-Field Skyrmions with a High Topological Number in Itinerant Magnets, Phys. Rev. Lett. **118**, 147205 (2017).

[33] S. Hayami, R. Ozawa, and Y. Motome, Effective bilinear-biquadratic model for noncoplanar ordering in itinerant magnet, Phys. Rev. B **95**, 224424 (2017).

[34] A. O. Leonov and M. Mostovoy, Multiply periodic states and isolated skyrmions in an anisotropic frustrated magnet, Nat. Commun. **6**, 8275 (2015).

[35] S. Hayami and Y. Motome, Effect of magnetic anisotropy on skyrmions with a high topological number in itinerant magnets, Phys. Rev. B **99**, 094420 (2019).

[36] Z. Wang, Y. Su, S.-Z. Lin, and C. D. Batista, Skyrmion Crystal from RKKY Interaction Mediated by 2D Electron Gas, Phys. Rev. Lett. **124**, 207201 (2020).

[37] O. I. Utesov, Thermodynamically stable skyrmion lattice in a tetragonal frustrated antiferromagnet with dipolar interaction, Phys. Rev. B **103**, 064414 (2021).

[38] J. A. M. Paddison, B. K. Rai, A. F. May, S. A. Calder, M. B. Stone, M. D. Frontzek, and A. D. Christianson, Magnetic Interactions of the Centrosymmetric Skyrmion Material Gd_2PdSi_3, Phys. Rev. Lett. **129**, 137202 (2022).

[39] D. S. Kathyat, A. Mukherjee, and S. Kumar, Electronic mechanism for nanoscale skyrmions and topological metals, Phys. Rev. B **103**, 035111 (2021).

[40] T. Nomoto, T. Koretsune, and R. Arita, Formation Mechanism of the Helical Q Structure in Gd-Based Skyrmion Materials, Phys. Rev. Lett. **125**, 117204 (2020).

[41] W. R. Meier, J. R. Torres, R. P. Hermann, J. Zhao, B. Lavina, B. C. Sales, and A. F. May, Thermodynamic insights into the intricate magnetic phase diagram of $EuAl_4$, Phys. Rev. B **106**, 094421 (2022).

[42] A. Nakamura, T. Uejo, F. Honda, T. Takeuchi, H. Harima, E. Yamamoto, Y. Hag, K. Matsubayashi, Y. Uwatoko, M. Hedo, T. Nakama, and Y. Ōnuki, Transport and magnetic properties of $EuAl_4$ and $EuGa_4$, J. Phys. Soc. Jpn. **84**, 124711 (2015).

[43] S. Shimomura, H. Murao, S. Tsutsui, H. Nakao, A. Nakamura, M. Hedo, T. Nakama, and Y. Ōnuki, Lattice modulation and structural phase transition in the antiferromagnet $EuAl_4$, J. Phys. Soc. Jpn. **88**, 014602 (2019).

[44] T. Shang, Y. Xu, D. J. Gawryluk, J. Z. Ma, T. Shiroka, M. Shi, and E. Pomjakushina, Anomalous Hall resistivity and possible topological Hall effect in the $EuAl_4$ antiferromagnet, Phys. Rev. B **103**, L020405 (2021).

[45] K. Kaneko, T. Kawasaki, A. Nakamura, K. Munakata, A. Nakao, T. Hanashima, R. Kiyanagi, T. Ohhara, M. Hedo, T. Nakama, and Y. Ōnuki, Charge-density-wave order and multiple magnetic transitions in divalent europium compound $EuAl_4$, J. Phys. Soc. Jpn. **90**, 064704 (2021).

[46] X. Y. Zhu, H. Zhang, D. J. Gawryluk, Z. X. Zhen, B. C. Yu, S. L. Ju, W. Xie, D. M. Jiang, W. J. Cheng, Y. Xu, M. Shi, E. Pomjakushina, Q. F. Zhan, T. Shiroka, and T. Shang, Spin order and fluctuations in the $EuAl_4$ and $EuGa_4$ topological antiferromagnets: A μSR study, Phys. Rev. B **105**, 014423 (2022).

[47] S. Hayami, Multiple skyrmion crystal phases by itinerant frustration in centrosymmetric tetragonal magnets, J. Phys. Soc. Jpn. **91**, 023705 (2022).

[48] S. Hayami, Rectangular and square skyrmion crystals on a centrosymmetric square lattice with easy-axis anisotropy, Phys. Rev. B **105**, 174437 (2022).

[49] See Supplemental Material at http://link.aps.org/supplemental/10.1103/PhysRevB.107.L020410 for details of experiments and analyses, which includes Refs. [50–52].

[50] R. Daou, F. Weickert, M. Nicklas, F. Steglich, A. Haase, and M. Doerr, High resolution magnetostriction measurements in pulsed magnetic fields using fiber Bragg gratings, Rev. Sci. Instrum. **81**, 033909 (2010).

[51] A. Miyake, M. Gen, A. Ikeda, K. Miyake, Y. Shimizu, Y. J. Sato, D. Li, A. Nakamura, Y. Homma, F. Honda, J. Flouquet, M. Tokunaga, and D. Aoki, Magnetovolume effect on the first-order metamagnetic transition in UTe_2, J. Phys. Soc. Jpn. **91**, 063703 (2022).

[52] M. Gen, A. Miyake, H. Yagiuchi, Y. Watanabe, A. Ikeda, Y. H. Matsuda, M. Tokunaga, T. Arima, and Y. Tokunaga, Enhancement of giant magnetoelectric effect in Ni-doped $CaBaCo_4O_7$, Phys. Rev. B **105**, 214412 (2022).

[53] J. Prokleška, J Vejpravová, and V Sechovský, Magnetostriction measurement of $GdRu_2Si_2$ single crystal, J. Phys.: Conf. Ser. **51**, 028 (2006).

[54] S. Ramakrishnan, S. R. Kotla, T. Rekis, J.-K. Bao, C. Eisele, L. Noohinejad, M. Tolkiehn, C. Paulmann, B. Singh, R. Verma, B. Bag, R. Kulkarni, A. Thamizhavel, B. Singh, S. Ramakrishnan, and S. van Smaalen, Orthorhombic charge density wave on the tetragonal lattice of $EuAl_4$, IUCrJ **9**, 378 (2022).

[55] M. Stavinoha, J. A. Cooley, S. G. Minasian, T. M. McQueen, S. M. Kauzlarich, C.-L. Huang, and E. Morosan, Charge density wave behavior and order-disorder in the antiferromagnetic metallic series $Eu(Ga_{1-x}Al_x)_4$, Phys. Rev. B **97**, 195146 (2018).

[56] H. Zhang, X. Y. Zhu, Y. Xu, D. J. Gawryluk, W. Xie, S. L. Ju, M. Shi, T. Shiroka, Q. F. Zhan, E. Pomjakushina, and T. Shang, Giant magnetoresistance and topological Hall effect in the $EuGa_4$ antiferromagnet, J. Phys.: Condens. Matter **34**, 034005 (2022).

[57] J. M. Moya, S. Lei, E. M. Clements, C. S. Kengle, S. Sun, K. Allen, Q. Li, Y. Y. Peng, A. A. Husain, M. Mitrano, Matthew J. Krogstad, R. Osborn, A. B. Puthirath, S. Chi, L. Debeer-

Schmitt, J. Gaudet, P. Abbamonte, J. W. Lynn, and E. Morosan, Incommensurate magnetic orders and topological Hall effect in the square-net centrosymmetric $EuGa_2Al_2$ system, Phys. Rev. Mater. **6**, 074201 (2022).

[58] We used different $EuAl_4$ crystals in the FBG and RXS experiments. In Fig. 4(d), the demagnetization correction is performed for the FBG data so that the transition fields H_{c1}–H_{c4} match those obtained in the RXS experiment.

[59] We adopt the Lorentzian function for the fundamental Bragg peaks and the Gaussian function for the magnetic Bragg peaks. In phases II–IV, we performed the $(H, K, 0)$ mesh scans in the vicinity of the magnetic Bragg reflections. For these two-dimensional (2D) data, we adopt the 2D-Gaussian fitting to estimate the peak positions and FWHMs for q_a and q_b.

[60] Z. Wang, Y. Su, S.-Z. Lin, and C. D. Batista, Meron, skyrmion, and vortex crystals in centrosymmetric tetragonal magnets, Phys. Rev. B **103**, 104408 (2021).

[61] A. E. Petrova and S. M. Stishov, Thermal expansion and magnetovolume studies of the itinerant helical magnet MnSi, Phys. Rev. B **94**, 020410(R) (2016).

[62] T. Takeuchi, M. Kakihana, M. Hedo, T. Nakama, and Y. Onuki, Magnetic field versus temperature phase diagram for $H \parallel [001]$ in the trillium lattice antiferromagnet EuPtSi, J. Phys. Soc. Jpn. **88**, 053703 (2019).

[63] S. Spachmann, A. Elghandour, M. Frontzek, W. Löser, and R. Klingeler, Magnetoelastic coupling and phases in the skyrmion lattice magnet Gd_2PdSi_3 discovered by high-resolution dilatometry, Phys. Rev. B **103**, 184424 (2021).

[64] K. Shibata, J. Iwasaki, N. Kanazawa, S. Aizawa, T. Tanigaki, M. Shirai, T. Nakajima, M. Kubota, M. Kawasaki, H. S. Park, D. Shindo, N. Nagaosa, and Y. Tokura, Large anisotropic deformation of skyrmions in strained crystal, Nat. Nanotechnol. **10**, 589 (2015).

[65] Y. Nii, A. Kikkawa, Y. Taguchi, Y. Tokura, and Y. Iwasa, Elastic Stiffness of a Skyrmion Crystal, Phys. Rev. Lett. **113**, 267203 (2014).

[66] A. E. Petrova and S. M. Stishov, Field evolution of the magnetic phase transition in the helical magnet MnSi inferred from ultrasound studies, Phys. Rev. B **91**, 214402 (2015).